PCCP

PAPER

View Article Online
View Journal | View Issue

Cite this: *Phys. Chem. Chem. Phys.*, 2017, **19**, 7964

Substrate and band bending effects on monolayer FeSe on $SrTiO_3$(001)

Meiling Xu,[ab] Xianqi Song[a] and Hui Wang*[a]

Received 10th January 2017,
Accepted 23rd February 2017

DOI: 10.1039/c7cp00173h

rsc.li/pccp

Motivated by the high superconducting transition temperature (T_C) shown by monolayer FeSe on cubic perovskite $SrTiO_3$(001) and $SrTiO_3$(001)-2×1 reconstructed surfaces, in this study, we explore the atomic and electronic structures of monolayer FeSe on various $SrTiO_3$(001)-2×1 surface reconstructions using the CALYPSO method and first-principles calculations. Our search reveals two new Ti_2O_2 and Ti_2O reconstructed surface structures, besides the Ti_2O_3 and double TiO_2 layer reconstructed surfaces, and the two new Ti_2O_2 and Ti_2O reconstructed surface structures are more stable under Ti-rich conditions than under Ti-poor conditions. The Fermi-surface topology of an FeSe monolayer on Ti_2O_3- and Ti_2O_2-type reconstructed STO surfaces is different from that of an FeSe monolayer on a Ti_2O-type STO reconstructed surface. The established structure of monolayer FeSe on a Ti_2O-type STO(001) reconstructed surface can naturally explain the experimental observation of the electronic band structure on the monolayer FeSe superconductor and obtained electrons counting per Fe atom. Surface states in the mid-gap induced by various STO surface reconstructions will result in band bending. The surface-state-induced band bending is also responsible for the electron transfer from the STO substrate to the FeSe films.

Introduction

The high-temperature superconductivity recently reported for monolayer FeSe films grown on TiO_2 terminated (001) surfaces of cubic perovskite $SrTiO_3$ (STO) substrates[1–4] [herein referred to as FeSe/STO(001)] has attracted much attention owing to the material's high superconducting transition temperature (T_C) and simple electronic structure. Considerable research has been devoted to exploring its underlying physical mechanism.[5–9] Such a high T_C is unexpected in the FeSe system, because bulk FeSe exhibits a T_C of 8 K at ambient pressure,[10] although it can be enhanced to ~37 K under high pressure.[11] When thin FeSe films grow on, for example, graphene/SiC(0001), the maximum T_C is that of bulk FeSe, and no superconducting gap on the monolayer FeSe is found.[12] However, the T_C is dramatically enhanced to 65–109 K on an FeSe/STO(001) substrate. This suggests that the substrate somehow raises the T_C. Scanning tunneling microscopy has shown the surface to be 2×1 reconstructed, which is in line with employing Se-etching to smooth the STO substrate.[1] Surface reconstruction will induce surface states in the band gap, which might influence the electronic properties or the T_C of the FeSe monolayer. Much work so far has focused on STO(001)-2×1 reconstructed surfaces through experimental and theoretical studies.[13–17]

Angle-resolved photoemission spectroscopy has shown there to be only electron pockets near the Fermi surfaces in superconducting monolayer FeSe/STO samples,[18] reminiscent of the Fermi surface of superconducting single-crystal $A_xFe_{2-y}Se_2$ (where A = K, Cs, Rb, Tl, *etc.*, and T_C ~ 27–30 K)[19,20] as well as that of $(Li_{1-x}Fe_x)OHFe_{1-y}Se$ (T_C = 41 K),[21,22] suggesting that the superconducting FeSe films are electron doped.[23,24] Photoelectron spectroscopy has also shown that, unlike other Fe-based superconductors,[25,26] the Fermi surface of single-layer FeSe on $SrTiO_3$ consists only of electron pockets at the zone corners, without any hole pockets around the zone center. These observations suggest that electron doping enhances T_C. However, this concept has recently been challenged by studies of high-temperature superconductivity in monolayer FeSe films on anatase TiO_2(001)[27] substrates, which have demonstrated that the O vacancy density at the interface has no effect on the FeSe morphology or the magnitude of the superconducting gap.

Charge transfer from the STO substrate is widely considered an important part of the conductivity of the FeSe system.[5,6,8] Understanding the origin of this charge transfer is indispensable to efforts to enhance T_C. It is widely believed that the doping originates from the oxygen vacancies present on the TiO_2 layer of the interface, but this is not yet proven, and few studies have examined the origin of charge transfer from the viewpoint of band bending (an approach expounded by Zhang *et al.*[28]).

[a] *State Key Lab of Superhard Materials, Jilin University, Changchun 130023, China. E-mail: huiwang@jlu.edu.cn*
[b] *Beijing Computational Science Research Center, Beijing 100084, China*

This work reports the results of extensive structure searches for STO(001)-2×1 surface reconstructions using the swarm-intelligence-based CALYPSO code in combination with first-principles total energy calculations to determine whether STO substrate reconstruction crucially influences superconductivity. Besides the known Ti_2O_3 and double TiO_2 layer reconstructed surfaces, our searches find new Ti_2O_2 and Ti_2O reconstructed surfaces which are more stable under Ti-rich conditions than under Ti-poor conditions. The Fermi-surface topology and obtained electrons per Fe atom of FeSe monolayer on the Ti_2O-type STO reconstructed surface are in good agreement with the observed electronic band structure and theoretical results.[24,29] The Fermi-surface topology of the FeSe monolayer on Ti_2O_3- and Ti_2O_2-type reconstructed STO surfaces is different from that of the FeSe monolayer on the Ti_2O-type STO reconstructed surface. The band bending induced from STO(001)-2×1 surface reconstruction is responsible for the charge transfer between the monolayer FeSe and the STO substrate.

Calculation details

Our systematic surface structure search considers the rutile(011) surface of TiO_2 using the swarm-intelligence-based CALYPSO (Crystal structure AnaLYsis by Particle Swarm Optimization) method and its eponymous code. This methodology has been widely applied to predict the stable and metastable structures of extended crystals, low-dimensional materials, reconstructed surfaces, and nanoclusters.[30–33] Our surface structure slab models typically consist of three regions: the bulk region and the unreconstructed and reconstructed surface regions (see ref. 31 for details). Only surface regions are structurally optimized. The surface structure contains a symmetrical slab of five layers including TiO_2 and SrO; the top region is relaxed, and there is a vacuum layer of 13 Å. This choice relies on a series of tests on the number of TiO_2 layers used and the height of the vacuum layer chosen, giving a good converged surface energy (~1 meV per atom). The surface structures can thus be efficiently explored, allowing for both structural and compositional variations. For adatoms, TiO_2, Ti_2O, Ti_2O_3, Ti_2O_2, and Ti_4O_8 are considered. The 6000 considered structures are ranked according to the calculated enthalpy, and low-energy structures are then selected for detailed study. Once we have the low-energy structures in hand, finer parameters are used for calculating surface energies. To obtain FeSe films on different STO(001)-2×1 surfaces, an at least eight-layer STO(001) slab including reconstructed layers as the substrate with a vacuum layer of >10 Å was used for structural relaxation without any constraints and for electronic structural calculations. The underlying structure relaxations and electronic calculations were performed with the plane-wave pseudopotential method as implemented in the VASP code.[34] The Perdew–Burke–Ernzerhof generalized gradient approximation[35] was chosen for the exchange–correlation functional. The electron–ion interaction is described by projector augmented-wave potentials[36] with $3p^6 3d^3 4s^1$, $2s^2 2p^4$, $4s^2 4p^6 5s^2$, $4s^2 4p^4$ and $3d^7 4s^1$ configurations treated as the valence electrons for Ti, O, Sr, Se and Fe respectively. The original vdW-DF functional[37] was chosen to describe vdW interactions in layered systems not included in the conventional density functional theory. An energy cutoff of 500 eV for the plane-wave expansion and fine Monkhorst–Pack k meshes with grid spacing of $2\pi \times 0.04$ Å^{-1} are chosen to ensure that all the enthalpy calculations are well converged. The accuracy of the total energies obtained within the framework of the density functional theory is in many cases sufficient to predict the stability of the structures.

Results and discussion

Surface energy calculations and structural stability

The surface energy determining the stability of a surface is defined as

$$\gamma = \frac{1}{N}\left(G_s - \sum_i N_i \mu_i\right)$$

where G_s is the Gibbs free energy of the slab, and N_i and μ_i are the number of excess atoms of the cleaved surface and the chemical potential for each species, respectively. N is equal to $m \times n$ for an $m \times n$ surface cell, and serves as a normalization factor. The surface free energy can also be expressed in terms of the excesses Γ of the components, which is given for component i with respect to component A as

$$\Gamma_i = \frac{1}{A_s}\left(N_i - N_A \frac{N_i^{bulk}}{N_A^{bulk}}\right)$$

We choose component A to be SrO, and introduce a surface excess of TiO_2 and O, in terms of which the surface free energy is now

$$\gamma = \frac{1}{2A_s}\left[\left(G_s - N_{SrO} g_{SrTiO_3}\right) - \mu_{TiO_2}\Gamma_{TiO_2} - \mu_O \Gamma_O\right]$$

where g_{SrTiO_3} is the Gibbs free energy of a bulk formula unit of $SrTiO_3$. Chemical potentials have the constraints: $\mu_O \leq \mu_{O_2}/2$, $\mu_{TiO_2} \leq E_{TiO_2}$, and $\mu_{TiO_2} + \mu_{SrO} = g_{SrTiO_3}$, where E_{TiO_2} is the internal energy of a bulk rutile TiO_2 unit cell. At $\mu_{TiO_2} = E_{TiO_2}$ the system is in equilibrium with TiO_2 and $SrTiO_3$, and at $\mu_{TiO_2} = g_{SrTiO_3} - \mu_{SrO}$ the system is in equilibrium with SrO and $SrTiO_3$. The surface excesses Γ_{TiO_2} and Γ_O for each surface are listed in Table 1. The computed surface energies of different stoichiometric surfaces with respect to the chemical potential of O at T = 1000 K in equilibrium with TiO_2 are shown in Fig. 1. Clearly, within most of the potential range of μ_O ($\Delta\mu_O \geq -4.24$ eV) the double layer reconstructed model possesses the lowest surface

Table 1 N_{SrO}, Γ_{TiO_2}, and Γ_O for slabs representing different surface structures. $A_S^{(1\times1)}$ is the area of one of the surfaces of a (1×1) terminated slab

Surface		N_{SrO}	$A_S^{(1\times1)}\Gamma_{TiO_2}$	$A_S^{(1\times1)}\Gamma_O$
2×1	Ti_2O_3	8	1/2	−1/2
	Ti_2O_2	8	1/2	−1
	Ti_2O	8	1/2	−3/2
	Double layer	6	3/2	0
	TiO_2	8	0	0

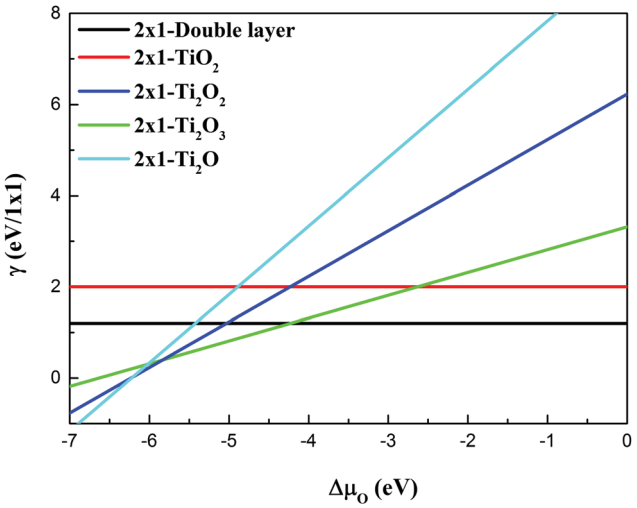

Fig. 1 Surface energies of various STO reconstructed surfaces with respect to $\Delta\mu_O$ at T = 1000 K in equilibrium with TiO_2.

energy; the Ti_2O_3-2×1 surface structure is stable within the $\Delta\mu_O$ range of −4.24 to −5.81; the Ti_2O_2-2×1 is energetically stable for $-5.81 > \Delta\mu_O \geq -6.22$; and Ti_2O is energetically stable for $-6.22 > \Delta\mu_O \geq -6.90$.

Structural parameters

The structures of the reconstructed stable surfaces with monolayer FeSe are shown in Fig. 2. The structure parameters and binding energies of FeSe/STO are listed in Table 2. Compared with the case of deposition on an unreconstructed surface, the FeSe layer sinks down toward the substrates with O vacancies, especially the Ti_2O-type substrate. The binding energies between the monolayer FeSe and the unreconstructed (0.78 eV) and double layer (0.73 eV) STO substrate (stoichiometric composition) in a 2×1 supercell are almost equal, while the value between the FeSe layer and the O-vacancy STO substrate is significantly higher. The binging energy increased with a decrease in the perpendicular average distance from Se atoms to Ti atoms. The binding energy between the monolayer FeSe and the Ti_2O-type substrates

Table 2 Summary of the main calculated results for the FeSe/STO film. Inter-dist. refers to the perpendicular average distance from Se atoms to Ti atoms. d is Se–Se bond length. The binding energy is per FeSe (2×1) cell according to our calculations

vdw = T	Unreconstructed	Double layer	Ti_2O_3-type	Ti_2O_2-type	Ti_2O-type
Inter-dist. (Å)	2.914	2.925	2.242	2.631	1.952
d_{Se-Se}	3.905	3.905	3.905	3.759	3.886
				4.051	3.943
E_{bind} (eV)	0.78	0.73	2.22	1.86	2.90

increases to 2.9 eV in a 2×1 supercell, and this strong binding is important in determining the growth mode of the FeSe films. The Coulomb force between monolayer FeSe and the positive charge left in STO is stronger in O-vacancy-type STO. There are two different spacings between the Se-atom rows on the top layer for the Ti_2O_2- and Ti_2O-types (about ∼4.0 Å and ∼3.8 Å, respectively), and the monolayer FeSe films exhibit a 2×1 reconstructed surface.

Electronic band structures

The calculated band structure of the bulk FeSe suggests that there are several hole pockets around the Γ point and two electron pockets around the M points, which is in close agreement with previous calculations.[38,39] Besides, we have made other band structure calculations of $\sqrt{2}a \times \sqrt{2}a$ STO(001) and the STO(110)-3×1 reconstructed surfaces and these results are in agreement with previous computational studies.[40,41] These results confirm the feasibility of our method. Important Fe, Se, Ti, and O fat-bands of FeSe/STO in a small energy window around E_F and the projected density of states in nonmagnetic states are calculated and shown in Fig. 3. The electronic structure near E_F is from Fe d bands (red line). As shown in Fig. 3(a), the Fermi surface of monolayer FeSe on an ideal STO surface is composed of two hole pockets around the Γ point, which is similar to that in bulk FeSe. As can be seen from Fig. 3(a), there is a bandgap about ∼0.7 eV between the partial density of states for Ti-d and O-p orbitals for the FeSe monolayer on the unreconstructed STO surface. This is in agreement

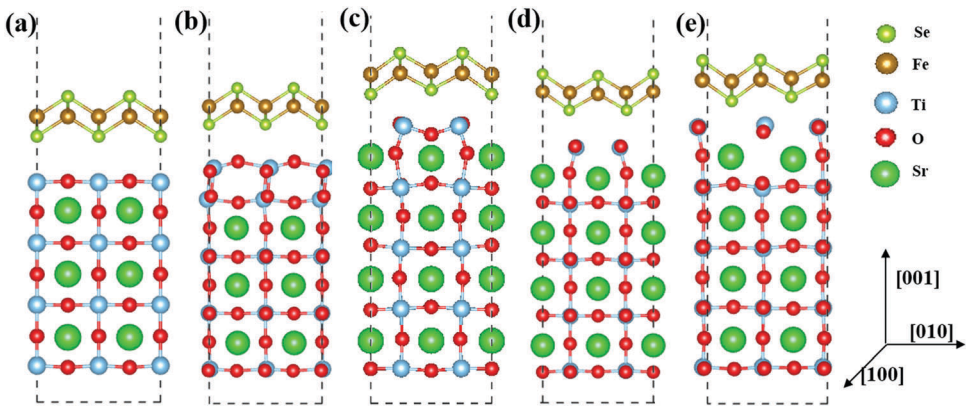

Fig. 2 Atomic structures of monolayer FeSe/STO(001) on various surface reconstructions. (a) Unreconstructed surface, and (b) double layer, (c) Ti_2O_3-, (d) Ti_2O_2-, and (e) Ti_2O-type reconstructed STO surfaces.

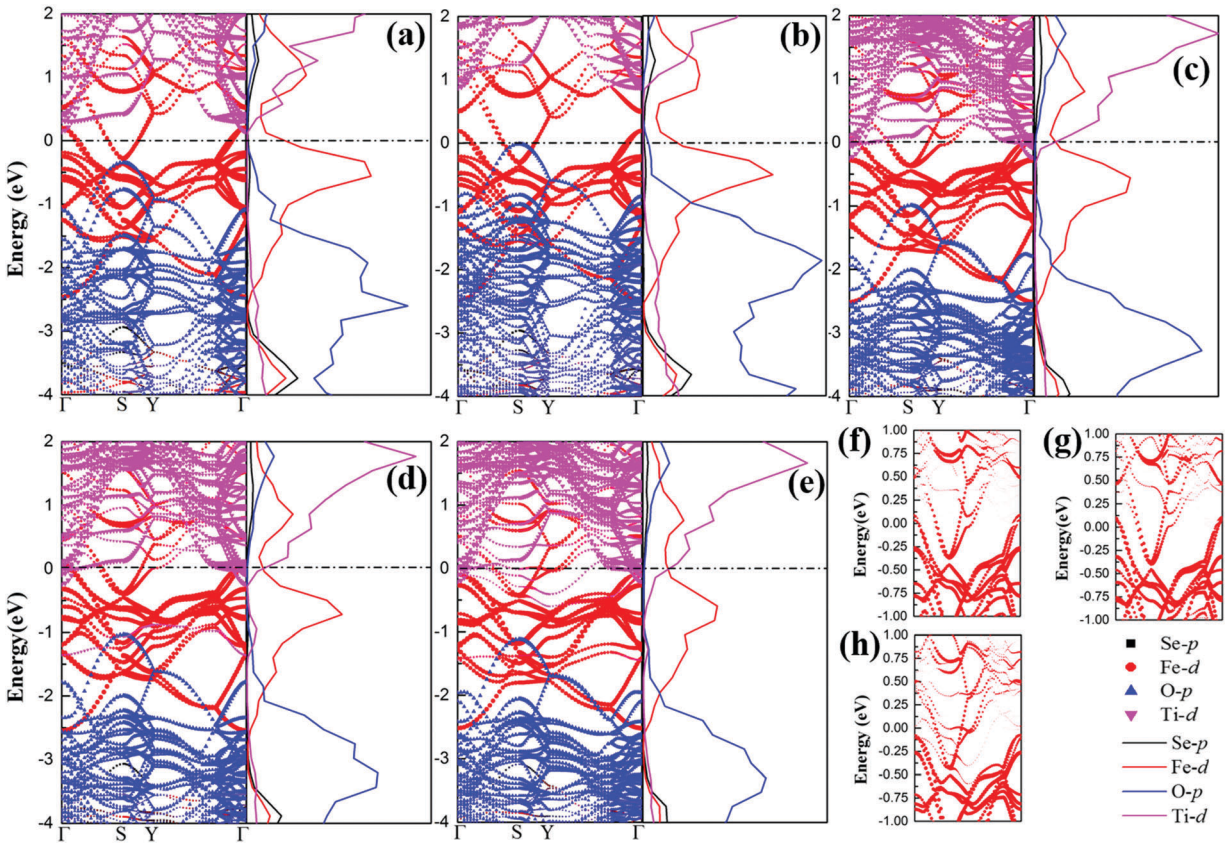

Fig. 3 Important Fe, Se, Ti, and O fat-bands of monolayer FeSe/STO in a small energy window around E_F and projected density of states in nonmagnetic states. (a) Unreconstructed surface, (b) double layer, (c)/(f) Ti_2O_3-, (d)/(g) Ti_2O_2-, and (e)/(h) Ti_2O-type reconstructed STO surfaces.

with the fact that STO is an insulator. When the STO reconstructed surface is stoichiometric [see Fig. 3(b)], the Fe d states are nearly the same as those of an unreconstructed STO surface. However, after deposition on an STO surface containing oxygen vacancies [see Fig. 3(c)–(e), (g) and (h)], the hole pockets at the Γ point of monolayer FeSe on a stoichiometric STO surface dip around or below the Fermi level, which suggests that O vacancies donate some electrons to the monolayer FeSe film. Therefore, hole pockets around the zone center in the bulk will disappear. Notably, no strong hybridization is found in the electronic states between the STO substrate and the FeSe film. Fig. 3(c)/(f) and (d)/(g) show that the Fermi-surface topologies of the FeSe monolayer of Ti_2O_3- and Ti_2O_2-type reconstructed STO substrates at the Fermi level around the Γ point are nearly the same. However, the hole pockets of monolayer FeSe on a stoichiometric STO surface at the Γ point with its top at 78 meV dip below the Fermi level for the Ti_2O-type reconstructed STO surface, which is in good agreement with the observed band structure of the monolayer FeSe superconductor.[24,29] The structure model of the FeSe monolayer on the Ti_2O-type reconstructed STO surface might be the experimental one, and might provide key insights into how to understand the superconductivity mechanism in the Fe-based superconductors. The Fermi-surface topology of the FeSe monolayer on Ti_2O_3- and Ti_2O_2-type reconstructed STO surfaces is different from that of the FeSe monolayer on the Ti_2O-type STO reconstructed one, suggesting that the STO reconstructed surfaces are likely to have an effect on high-temperature superconductivity in these systems.

Charge density difference

In order to obtain more insight into the charge transfer in the monolayer FeSe adsorbed on the various surface structures of STO, the charge density difference is obtained by subtracting the valence charge densities of the isolated FeSe monolayer and STO substrate from that of the combined system for the monolayer FeSe/STO(001)-2×1 reconstructed interface [Q = Q(FeSe/STO) − Q(STO) − Q(FeSe)]. In Fig. 4, we can find that doped electrons are mainly distributed at the interface from the spatial distribution of charge carriers. Meanwhile, the adsorption of the FeSe monolayer on the substrate induces a charge redistribution around Fe atoms. For the unreconstructed surface and the double layer reconstructed one, there is little electron transfer from the STO substrate to the Fe atoms. Charge transfer from the Ti_2O_3-, Ti_2O_2-, and Ti_2O-type STO surfaces to the FeSe layer can be clearly seen. The average charge of Fe atoms is about ∼0.04 eV, 0.05 eV, and 0.14 eV, respectively. This indicates a good agreement between the calculated charge difference density and fat-band structure calculations. An obtained electron count of about 0.14 electrons per Fe for monolayer FeSe on the Ti_2O-type reconstructed STO surface is also in agreement with the experimental and theoretical results,[24] which also supports that the structure model of the FeSe monolayer on Ti_2O-type

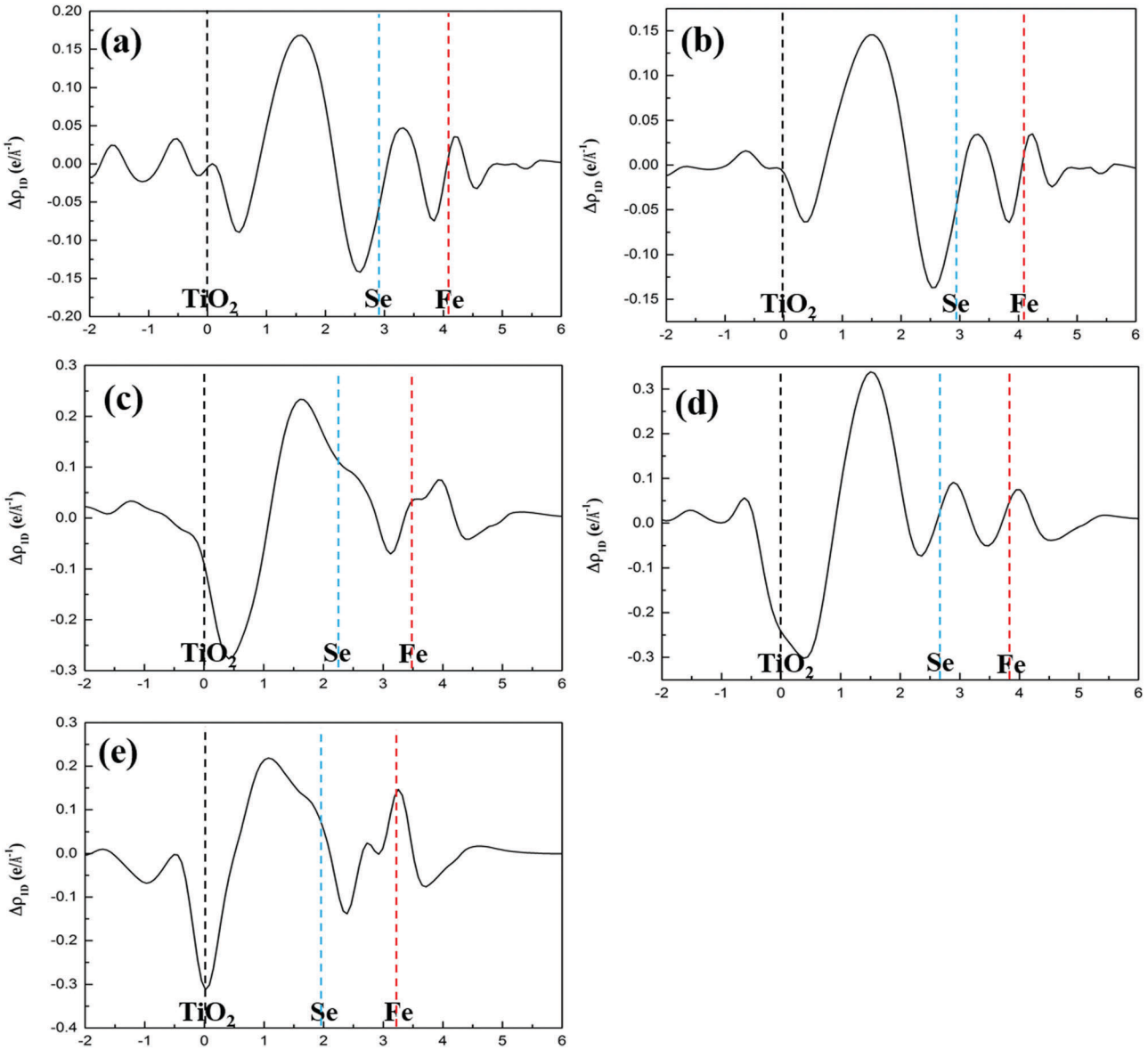

Fig. 4 The charge density difference obtained by subtracting the valence charge densities of the isolated FeSe layer and STO substrate from that of the combined system for the monolayer FeSe/STO(001)-2×1 reconstructed interface. The positions of the surface TiO_2 reconstructed layer of STO substrate and FeSe atomic layers are denoted by the dotted vertical colorful lines. (a) Unreconstructed surface, (b) double layer, (c) Ti_2O_3-, (d) Ti_2O_2-, and (e) Ti_2O-type reconstructed STO surfaces.

reconstructed STO surface might be the experimental one. It should be pointed out that although O vacancies donate some electrons to the monolayer FeSe, electron transfer dose not increase with oxygen vacancy densities from Fig. 3(c)/(f), (d)/(g) and 4 (c), (d). The reasons for this are very complicated. It is important to highlight that surface reconstruction will result in surface states in the mid-gap, which can be seen from Fig. 3(d) and (e) (Ti_d states in the mid-gap). The band bending induced by surface states is responsible for the electron transfer.

Band bending effects

Fig. 3(d) and (e) shows the surface states (Ti d states) obviously induced by surface reconstruction in the Ti_2O_2- and Ti_2O-type substrates. Surface states can result in band bending, which is schematically illustrated in ref. 28. Here, a brief introduction is given. We assume that the surface is half filled and located in the mid-gap. An intrinsic semiconductor has the Fermi level of the bulk centred at the middle of the gap, and its Fermi level is equal to that of the surface; consequently, there are no electrons to transfer between the bulk and surface. An n-type semiconductor has its Fermi level close to the conduction band, and charge will transfer from the bulk to the surface until an equilibrium is reached. The Fermi level of a p-type semiconductor is close to the valence band, and the electrons will transfer from the surface to the bulk. At equilibrium, the bands bend upward and downward, respectively, for the two types (see ref. 28 for details).

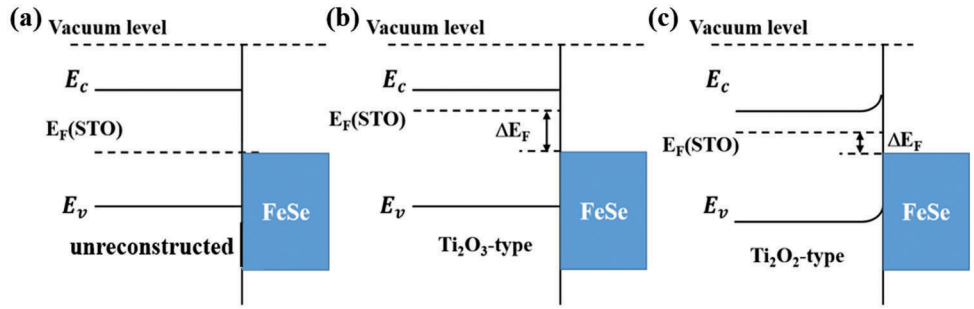

Fig. 5 Schematic of band bending in disequilibrium. Monolayer FeSe deposited on (a) the unreconstructed, (b) Ti_2O_3-type, and (c) Ti_2O_2-type STO reconstructed surfaces. ΔE_F is the relative difference between the Fermi level of STO and the Fermi level of the FeSe monolayer.

When a metal and semiconductor are in electronic contact, free electrons will transfer between them due to their different work functions.[42] If the work function of the metal is larger than that of the semiconductor, the electrons will transfer from the semiconductor to the metal until the Fermi energy of the former is equal to that of the latter. The flow will be reversed if the semiconductor has higher work function. The FeSe/STO substrate can be considered as a metal–semiconductor contact. When the FeSe (metal) and STO (semiconductor) are in contact, free electrons will transfer between them due to the work function difference. The stoichiometric STO surface reconstructions could be seen as intrinsic semiconductors, while the reconstructed STO surfaces with O vacancies could be treated as n-type semiconductors. We assume that the Fermi level of monolayer FeSe is equal to that of stoichiometric reconstructed STO surfaces, so there is no charge transfer between the monolayer FeSe and the stoichiometric reconstructed STO surfaces [see Fig. 5(a)]. However, when the reconstructed structure is reduced, the semiconductor STO is n-type and the Fermi level is close to the conduction band, so the electrons would diffuse into the monolayer FeSe from the Ti atoms bordering oxygen vacancies [see Fig. 5(b)]. This indicates a good agreement with the calculated band structure in Fig. 3(c), which shows that the hole pockets at the Γ point of monolayer FeSe on a Ti_2O_3 surface dip around the Fermi level, because O vacancies donate some electrons to the monolayer FeSe film.

Increasing the concentration of free charge carriers in the STO surface should cause the monolayer FeSe to obtain more electrons. However, this is not the case from the fat-band structure calculations of the Ti_2O_3- and Ti_2O_2-type substrates. As shown in Fig. 3(d), there are Ti surface states in the band gap for Ti_2O_2-type surface reconstructions. These surface states will induce band bending of the STO substrate, then affect electron transfer between the monolayer FeSe and the STO substrate. Fig. 5(c) shows that surface states induce the band edges to shift upward toward the surface until the Fermi level of the bulk equals that of the surface states. In this condition, the relative difference between the Fermi levels, ΔE_F, of the FeSe monolayer and Ti_2O_2-type reconstructed surfaces decreases compared with that of Ti_2O_3-type surface reconstruction. Therefore, a Ti_2O_2-type reconstructed surface does not provide more electrons to the FeSe monolayer because of surface-state-induced band bending, meaning that the charge transfer from the STO substrate to monolayer FeSe will be affected by band bending.

Conclusions

Unbiased swarm structure searches and density functional total energy calculations were performed to explore the atomic structures of different STO(001)-2×1 reconstructed surfaces. Our search reveals new Ti_2O_2 and Ti_2O reconstructed surface structures that are more stable under Ti-rich conditions than under Ti-poor conditions. There is excellent mutual agreement between experiments and theory in terms of the electronic band structure and obtained electrons counting per Fe atom, supporting the structure of monolayer FeSe on the Ti_2O-type STO(001) reconstructed surface as the likely structure of the experimental one, providing key insights into how to understand the superconductivity mechanism in the Fe-based superconductors. The Fermi-surface topology of the FeSe monolayer on Ti_2O_3- and Ti_2O_2-type reconstructed STO surfaces is different from that of the FeSe monolayer on a Ti_2O-type STO reconstructed one, suggesting the STO reconstructed surfaces are likely to have an effect on high-temperature superconductivity in these systems. Band bending induced by STO(001)-2×1 surface reconstruction is responsible for the charge transfer between monolayer FeSe and the STO substrate.

Acknowledgements

The authors thank the financial support by National Natural Science Foundation of China (under Grants No. 11474128, 11534003, and 11274136), and China 973 Program under Grant No. 2011CB808200. The calculations were performed in the computing facilities at the High Performance Computing Center of Jilin University.

References

1 Q.-Y. Wang, Z. Li, W.-H. Zhang, Z.-C. Zhang, J.-S. Zhang, W. Li, H. Ding, Y.-B. Ou, P. Deng, K. Chang, J. Wen, C.-L. Song, K. He, J.-F. Jia, S.-H. Ji, Y.-Y. Wang, L.-L. Wang,

X. Chen, X.-C. Ma and Q.-K. Xue, *Chin. Phys. Lett.*, 2012, **29**, 037402.
2 D. Liu, W. Zhang, D. Mou, J. He, Y.-B. Ou, Q.-Y. Wang, Z. Li, L. Wang, L. Zhao, S. He, Y. Peng, X. Liu, C. Chen, L. Yu, G. Liu, X. Dong, J. Zhang, C. Chen, Z. Xu, J. Hu, X. Chen, X. Ma, Q. Xue and X. J. Zhou, *Nat. Commun.*, 2012, **3**, 931.
3 J. Ge, Z.-L. Liu, C. Liu, C. Gao, D. Qian, Q. Xue, Y. Liu and J.-F. Jia, *Nat. Mater.*, 2014, **14**, 285–289.
4 Y. Sun, W. Zhang, Y. Xing, F. Li, Y. Zhao, Z. Xia, L. Wang, X. Ma, Q.-K. Xue and J. Wang, *Sci. Rep.*, 2014, **4**, 6040.
5 J. Bang, Z. Li, Y. Y. Sun, A. Samanta, Y. Y. Zhang, W. Zhang, L. Wang, X. Chen, X. Ma, Q.-K. Xue and S. B. Zhang, *Phys. Rev. B: Condens. Matter Mater. Phys.*, 2013, **87**, 220503.
6 T. Bazhirov and M. Lou Cohen, *J. Phys.: Condens. Matter*, 2013, **25**, 105506.
7 T. Berlijn, H.-P. Cheng, P. J. Hirschfeld and W. Ku, *Phys. Rev. B: Condens. Matter Mater. Phys.*, 2014, **89**, 020501.
8 I. Božović, *Nat. Phys.*, 2016, **12**, 22–24.
9 H.-Y. Cao, S. Chen, H. Xiang and X.-G. Gong, *Phys. Rev. B: Condens. Matter Mater. Phys.*, 2015, **91**, 020504.
10 F.-C. Hsu, J.-Y. Luo, K.-W. Yeh, T.-K. Chen, T.-W. Huang, P. M. Wu, Y.-C. Lee, Y.-L. Huang, Y.-Y. Chu, D.-C. Yan and M.-K. Wu, *Proc. Natl. Acad. Sci. U. S. A.*, 2008, **105**, 14262–14264.
11 S. Margadonna, Y. Takabayashi, Y. Ohishi, Y. Mizuguchi, Y. Takano, T. Kagayama, T. Nakagawa, M. Takata and K. Prassides, *Phys. Rev. B: Condens. Matter Mater. Phys.*, 2009, **80**, 1–6.
12 C. L. Song, Y. L. Wang, Y. P. Jiang, Z. Li, L. Wang, K. He, X. Chen, X. C. Ma and Q. K. Xue, *Phys. Rev. B: Condens. Matter Mater. Phys.*, 2011, **84**, 2–5.
13 M. R. Castell, *Surf. Sci.*, 2002, **505**, 1–13.
14 N. Erdman, K. R. Poeppelmeier, M. Asta, O. Warschkow, D. E. Ellis and L. D. Marks, *Nature*, 2002, **419**, 55–58.
15 R. Herger, P. R. Willmott, O. Bunk, C. M. Schlepütz, B. D. Patterson and B. Delley, *Phys. Rev. Lett.*, 2007, **98**, 076102.
16 R. Herger, P. R. Willmott, O. Bunk, C. M. Schlepütz, B. D. Patterson, B. Delley, V. L. Shneerson, P. F. Lyman and D. K. Saldin, *Phys. Rev. B: Condens. Matter Mater. Phys.*, 2007, **76**, 195435.
17 O. Warschkow, M. Asta, N. Erdman, K. R. Poeppelmeier, D. E. Ellis and L. D. Marks, *Surf. Sci.*, 2004, **573**, 446–456.
18 S. Tan, Y. Zhang, M. Xia, Z. Ye, F. Chen, X. Xie, R. Peng, D. Xu, Q. Fan, H. Xu, J. Jiang, T. Zhang, X. Lai, T. Xiang, J. Hu, B. Xie and D. Feng, *Nat. Mater.*, 2013, **12**, 634.
19 T. Qian, X.-P. Wang, W.-C. Jin, P. Zhang, P. Richard, G. Xu, X. Dai, Z. Fang, J.-G. Guo, X.-L. Chen and H. Ding, *Phys. Rev. Lett.*, 2011, **106**, 187001.
20 Y. Zhang, L. X. Yang, M. Xu, Z. R. Ye, F. Chen, C. He, H. C. Xu, J. Jiang, B. P. Xie, J. J. Ying, X. F. Wang, X. H. Chen, J. P. Hu, M. Matsunami, S. Kimura and D. L. Feng, *Nat. Mater.*, 2011, **10**, 273–277.
21 X. F. Lu, N. Z. Wang, H. Wu, Y. P. Wu, D. Zhao, X. Z. Zeng, X. G. Luo, T. Wu, W. Bao, G. H. Zhang, F. Q. Huang, Q. Z. Huang and X. H. Chen, *Nat. Mater.*, 2014, **14**, 325–329.
22 L. Zhao, A. Liang, D. Yuan, Y. Hu, D. Liu, J. Huang, S. He, B. Shen, Y. Xu, X. Liu, L. Yu, G. Liu, H. Zhou, Y. Huang, X. Dong, F. Zhou, K. Liu, Z. Lu, Z. Zhao, C. Chen, Z. Xu and X. J. Zhou, *Nat. Commun.*, 2016, **7**, 10608.
23 S. He, *Nat. Mater.*, 2013, **12**, 605–610.
24 D. Liu, W. Zhang, D. Mou, J. He, Y.-B. Ou, Q.-Y. Wang, Z. Li, L. Wang, L. Zhao, S. He, Y. Peng, X. Liu, C. Chen, L. Yu, G. Liu, X. Dong, J. Zhang, C. Chen, Z. Xu, J. Hu, X. Chen, X. Ma, Q. Xue and X. J. Zhou, *Nat. Commun.*, 2012, **3**, 931.
25 L. Zhao, H. Liu, W. Zhang and J. Meng, *et al.*, *Chin. Phys. Lett.*, 2008, **25**(12), 4402.
26 D. Mou, S. Liu, X. Jia, J. He, Y. Peng, L. Zhao, L. Yu, G. Liu, S. He, X. Dong, J. Zhang, H. Wang, C. Dong, M. Fang, X. Wang, Q. Peng, Z. Wang, S. Zhang, F. Yang, Z. Xu, C. Chen and X. J. Zhou, *Phys. Rev. Lett.*, 2011, **106**, 107001.
27 H. Ding, Y. F. Lv, K. Zhao, W. L. Wang, L. Wang, C. L. Song, X. Chen, X. C. Ma and Q. K. Xue, *Phys. Rev. Lett.*, 2016, **117**, 1–5.
28 Z. Zhang and J. T. Yates, *Chem. Rev.*, 2012, **112**, 5520–5551.
29 J. J. Lee, F. T. Schmitt, R. G. Moore, S. Johnston, Y.-T. Cui, W. Li, M. Yi, Z. K. Liu, M. Hashimoto, Y. Zhang, D. H. Lu, T. P. Devereaux, D.-H. Lee and Z.-X. Shen, *Nature*, 2014, **515**, 245–248.
30 Y. Wang, J. Lv, L. Zhu and Y. Ma, *Comput. Phys. Commun.*, 2012, **183**, 2063–2070.
31 S. Lu, Y. Wang, H. Liu, M.-S. Miao and Y. Ma, *Nat. Commun.*, 2014, **5**, 3666.
32 J. Lv, Y. Wang, L. Zhu and Y. Ma, *Phys. Rev. Lett.*, 2011, **106**(1), 015503.
33 Y. Wang, J. Lv, L. Zhu and Y. Ma, *Phys. Rev. B: Condens. Matter Mater. Phys.*, 2010, **82**, 094116.
34 G. Kresse and J. Hafner, *Phys. Rev. B: Condens. Matter Mater. Phys.*, 1994, **49**, 14251–14269.
35 J. P. Perdew, K. Burke and M. Ernzerhof, *Phys. Rev. Lett.*, 1996, **77**, 3865–3868.
36 P. E. Blöchl, *Phys. Rev. B: Condens. Matter Mater. Phys.*, 1994, **50**, 17953–17979.
37 J. Klimeš, D. R. Bowler and A. Michaelides, *Phys. Rev. B: Condens. Matter Mater. Phys.*, 2011, **83**, 195131.
38 A. Subedi, L. Zhang, D. J. Singh and M. H. Du, *Phys. Rev. B: Condens. Matter Mater. Phys.*, 2008, **78**, 1–6.
39 H. Cao, S. Tan, H. Xiang, D. L. Feng and X. Gong, *Phys. Rev. B: Condens. Matter Mater. Phys.*, 2014, **89**, 014501.
40 X. Wu, X. Dai, Y. Liang, C. Le, H. Fan and J. Hu, *Phys. Rev. B: Condens. Matter Mater. Phys.*, 2016, **94**, 045114.
41 K. Liu, Z.-Y. Lu and T. Xiang, *Phys. Rev. B: Condens. Matter Mater. Phys.*, 2012, **85**, 235123.
42 W. Mönch, *Surf. Sci.*, 1994, **299–300**, 928–944.

